Draft version March 22, 2024
Typeset using LaTeX **twocolumn** style in AASTeX631

Elements formation in radiation-hydrodynamics simulations of kilonovae

Fabio Magistrelli,[1] Sebastiano Bernuzzi,[1] Albino Perego,[2,3] and David Radice[4,5,6,*]

[1] *Theoretisch-Physikalisches Institut, Friedrich-Schiller-Universität Jena, 07743, Jena, Germany*
[2] *Dipartimento di Fisica, Università di Trento, Via Sommarive 14, 38123 Trento, Italy*
[3] *INFN-TIFPA, Trento Institute for Fundamental Physics and Applications, via Sommarive 14, I-38123 Trento, Italy*
[4] *Institute for Gravitation & the Cosmos, The Pennsylvania State University, University Park, PA 16802*
[5] *Department of Physics, The Pennsylvania State University, University Park, PA 16802*
[6] *Department of Astronomy & Astrophysics, The Pennsylvania State University,University Park, PA 16802*

(Dated: March 22, 2024)

ABSTRACT

Understanding the details of r-process nucleosynthesis in binary neutron star mergers (BNSMs) ejecta is key to interpret kilonovae observations and to identify the role of BNSMs in the origin of heavy elements. We present a self-consistent 2-dimensional (ray-by-ray) radiation-hydrodynamic evolution of BNSM ejecta with an online nuclear network (NN) up to the days timescale. For the first time, an initial numerical-relativity ejecta profile composed of the dynamical component, spiral-wave and disk winds is evolved including detailed r-process reactions and nuclear heating effects. A simple model for the jet energy deposition is also included. Our simulation highlights that the commonly assumed approach of relating the final nucleosynthesis yields to the initial thermodynamic profile of the ejecta can lead to inaccurate predictions. We also find significant deviations (up to four orders of magnitudes) in the abundance evolution of several analyzed elements compared to previous predictions employing the NN in post-processing. The presence of a jet affects elements production only in the innermost part of the polar ejecta, and it does not alter the global nucleosynthesis results. Overall, our analysis shows that employing an online NN is highly desiderable in order to obtain reliable predictions of r-process nucleosynthesis and ejecta evolution.

1. INTRODUCTION

Mass ejecta from binary neutron star mergers (BNSMs) are primary sites for rapid neutron capture (r-process) nucleosynthesis (Eichler et al. 1989), see *e.g.* (Cowan et al. 2021; Perego et al. 2021; Arcones & Thielemann 2023). The heavy, neutron-rich elements produced in these environments undergo radioactive decays, powering an electromagnetic (EM) transient known as a kilonova. Moreover, some of these mergers can produce short gamma-ray bursts (sGRBs), offering further insights into their astrophysical properties. The unambiguous detection of gravitational waves (GW170817) and EM counterparts (kilonova AT2017gfo and GRB 170817A) from a BNSM in August 2017 has confirmed theoretical predictions and triggered intense work on the subject (Abbott et al. 2017a,b,c; Coulter et al. 2017; Tanvir et al. 2017; Savchenko et al. 2017).

Numerical simulations are the main tool to explore the physics of BNSMs and identify the mechanisms underlying the associated gravitational and EM emissions (Bauswein et al. 2013; Rosswog et al. 2014; Roberts et al. 2017; Shibata et al. 2017; Nedora et al. 2021; Radice et al. 2022; Zappa et al. 2023; Combi & Siegel 2023a,b; Schianchi et al. 2023; Radice & Bernuzzi 2023a; Musolino et al. 2024). Simulations are used to carry out extensive investigations on r-process nucleosynthesis and

fabio.magistrelli@uni-jena.de
sebastiano.bernuzzi@uni-jena.de
albino.perego@unitn.it
david.radice@psu.edu
* Alfred P. Sloan fellow

its relationship with kilonovae. Lanthanides and actinides production is consistently found in low electron fraction ejected material ($Y_e \lesssim 0.2$) (Korobkin et al. 2012; Lippuner & Roberts 2015; Perego et al. 2021). Low values of Y_e can be found in the equatorial component of dynamical ejecta (Goriely et al. 2011; Wanajo et al. 2014; Sekiguchi et al. 2016; Radice et al. 2016) and in the late disk wind, *e.g.* (Beloborodov 2003; Siegel & Metzger 2017; Sprouse et al. 2023). The high opacity associated with these elements commonly links the outer regions of the (low-latitude) ejecta with the red component of the kilonova light curves (Metzger & Fernández 2014; Perego et al. 2017). However, small expansion timescales can inhibit neutron captures and thus produce a blue-UV precursor powered by decays of free neutrons (Metzger et al. 2015; Radice et al. 2018a; Combi & Siegel 2023a). Higher values of $Y_e \gtrsim 0.3$ associated with most of the disk and the majority of polar ejecta prevent strong r-processes, thus leading to low opacity matter contributing to the blue part of the kilonova spectra (Metzger & Fernández 2014; Kasen et al. 2017; Tanaka et al. 2017; Curtis et al. 2024). In the polar regions, this is enhanced by interactions with neutrinos emitted by the central remnant until its possible collapse to a black hole (Radice & Bernuzzi 2023b). The passage of a relativistic jet can in principle affect the nucleosynthesis by injecting extra energy in the system and thus reigniting suppressed reactions (Janiuk 2014). Understanding the details of the nuclear evolution of the ejecta and how this affects its dynamics is crucial for accurately interpreting observational data and assessing the role of BNSMs in explaining the origin of r-process elements in the universe.

One of the main open challenges towards the accurate prediction of r-process nucleosynthesis in BNSMs ejecta is capturing the dependence of the nuclear composition outcomes on the initial thermodynamic profile and detailed hydrodynamic evolution of the ejecta. Traditional approaches assume homologously expanding ejecta profiles and neglect radiation transport, hydrodynamics and ejecta self-interaction, *e.g.* (Korobkin et al. 2012; Radice et al. 2016; Rosswog et al. 2017; Perego et al. 2022; Curtis et al. 2024), although some recent efforts have considered detailed radiation transport, *e.g.* (Collins et al. 2023; Shingles et al. 2023). Alternatively, nuclear networks are employed in a post-processing step on hydrodynamics profiles to obtain yields and heating rates (Just et al. 2015; Martin et al. 2015; Goriely 2015; Roberts et al. 2017). The latter are sometimes fitted as time-domain functions and reused in hydrodynamical simulations to improve ejecta evolutions, *e.g.* (Rosswog et al. 2014; Wu et al. 2022; Ricigliano et al. 2023).

In this work, we present, for the first time, a self-consistent simulation of r-process nucleosynthesis for a fiducial BNSM ejecta using a 2-dimensional, ray-by-ray radiation hydrodynamics code coupled with an online nuclear network (NN). In Section 2, we present our model and discuss how the NN is coupled with the radiation-hydrodynamic equations to update the ejecta composition and calculate the associated nuclear power in each hydrodynamic step. We also describe our implementation of thermalization processes and of an extra energy source modeling a sGRB. Section 3 presents the nucleosynthesis and kilonova light curves predictions from the ejecta profiles we extract form a fiducial BNSM numerical relativity simulation. In Section 4, we conclude discussing the implications of our findings and emphasizing the importance of implementing an online NN for self-consistent predictions of r-process nucleosynthesis patterns.

2. METHOD

2.1. *Numerical-relativity profiles*

Our simulation is initialized with initial ejecta profiles extracted from ab-initio numerical relativity simulations that include microphysics, M0 neutrino transport[1] and magnetic-field induced turbulence (Radice et al. 2018b; Perego et al. 2019; Bernuzzi 2020; Nedora et al. 2021). The considered binary has mass ratio $q = 1.43$ and produces a short-lived remnant that collapses to a black hole (BH) at about 10 ms postmerger. The simulation is run with the LS220 equation of state (EoS) and with a typical resolution of 185m (Nedora et al. 2021). Throughout the simulation, the unbound material is identified via the Bernoulli criterion and collected at an extraction radius of $R_{\rm ext} \simeq 295$ km. The ejecta consists of the dynamical component of mass $\sim 1.24 \times 10^{-2}$ $M_\odot$ and a short spiral-wave wind ($\sim 0.80 \times 10^{-2}$ $M_\odot$). In order to prepare the subsequent long-term evolution, the dependence of the ejecta properties on the azimuthal coordinate is integrated out, while the polar dependence is accounted for by discretizing the polar angle in 51 angular sections. The time-dependent ejecta profile is mapped to a Lagrangian profile by positioning the latest shell at $R_{\rm ext}$ and progressively layering previously ejected shells on top as prescribed by the constraint $m(r) = 4\pi \int_{R_{\rm ext}}^{r} \rho(r)\, r^2 dr$, with ρ mass density and r position of the radius including the mass m (Wu

[1] See Zappa et al. (2023) for the importance of including neutrino heating effects.

et al. 2022). An analytical disk wind profile of mass $\sim 2.75 \times 10^{-2}$ $M_\odot$ is instead constructed from a similar simulation but performed on an equal mass binary with the M1 neutrino transport (Radice et al. 2022), which better describes the optically thick regime (Zappa et al. 2023). The simulation of the $q = 1$ binary is run with the SFHo EoS for ∼270 ms postmerger[2]. The disk profile is constructed by interpolating the spherically averaged density, temperature, and electron fraction of the unbound matter over time and using second-order Padé approximants. We assume a constant velocity and entropy, and rescale the density evolution to get a total ejection of 40% of the total disk mass assuming a $\propto \sin^2\theta$ angular distribution (Perego et al. 2017; Fernández et al. 2019). The complete initial profiles of two selected angular sections are shown in the two bottom panels of Fig. 1.

2.2. *Ray-by-ray Radiation-Hydrodynamics*

The ejecta profile is evolved with the system of Lagrangian radiation-hydrodynamic equations as implemented in Morozova et al. (2015); Wu et al. (2022). In particular, the energy equation in spherical symmetry reads

$$\frac{\partial \epsilon}{\partial t} = \frac{P}{\rho}\frac{\partial \ln \rho}{\partial t} - 4\pi r^2 Q \frac{\partial v}{\partial m} - \frac{\partial L}{\partial m} + \dot{\epsilon}_{\rm nucl}\,, \qquad (1)$$

with m mass coordinate, ϵ specific internal energy, t time, P pressure, v (radial) velocity, L luminosity and Q von Neumann-Richtmyer artificial viscosity (Von Neumann & Richtmyer 1950). The specific energy deposition $\dot{\epsilon}_{\rm nucl}$ accounts for the local production and partial thermalization of the energy released by all possible nuclear reactions occurring in the expanding material. To calculate the luminosity, we employ the same analytic, time-independent opacity introduced in Wu et al. (2022).

The set of hydrodynamic equations is closed by the EoS. In the high-temperature regime, we implement the tabulated Helmholtz EoS introduced in Timmes & Swesty (2000) and also used in Lippuner & Roberts (2017). For lower temperatures, where the contribution of positrons is negligible, we switch to the Paczynski EoS introduced in Paczynski (1986) and utilized in Morozova et al. (2015); Wu et al. (2022). This analytical EoS describes a mixture of ideal gases, namely a Boltzmann gas of non-degenerate, non-relativistic ions, an ideal gas of arbitrarily degenerate and relativistic electrons, and a photon ideal gas. The inclusion of an online nuclear network, as described in Sec. 2.3, improves the realism of these EoS, as the mean molecular weight and the electron fraction, which enter the EoS, are self-consistently calculated on the fly.

To account for the angular dependency of the ejecta properties, we employ the spherically symmetric hydrodynamic equations in a ray-by-ray fashion. For each angular section, we first map the profile into an effective 1D problem by multiplying the total mass by the scaling factor $\lambda_\theta = 4\pi/\Delta\Omega$, where $\Delta\Omega \simeq 2\pi \sin\theta\, d\theta$ represents the solid angle included in the angular section. This ensures that all the intensive quantities (including density) remain fixed. Then, we independently evolve the different angular sections by discretizing the 1D hydrodynamic equations over $n_{\rm sh} = 600$ spherical fluid elements (mass shells). Non-radial flows of matter and radiation are neglected. Finally, we map the problem back to the axisymmetric scenario by keeping the intensive quantities unchanged, rescaling the extensive ones by the scaling factor $1/\lambda_\theta$ and combining the results. In particular, we calculate the global mass fractions and abundances with a mass weighted average over all the mass shells and angular sections. Kilonova light curves are recombined accounting for the angle of view as in Martin et al. (2015); Perego et al. (2017).

2.3. *Nuclear Network Coupling*

We calculate the nuclear composition and specific energy deposition, $\dot{\epsilon}_{\rm nucl}$, in a self-consistent way with an online implementation of the nuclear network (NN) `SkyNet` (Lippuner & Roberts 2017). The NN includes 7836 isotopes up to ^{337}Cn and uses the JINA REACLIB (Cyburt et al. 2010) and the same setup as in Lippuner & Roberts (2015); Perego et al. (2022). The simulation is started by initializing matter composition from the initial temperature $T_0(m)$ and density $\rho_0(m)$ assuming nuclear statistical equilibrium (NSE). We thus impose, to each isotope considered in the NN, the abundance (Cowan et al. 2021; Perego et al. 2021)

$$Y_{i,0} = \frac{n_{i,0}}{n_{b,0}} = Y_{p,0}^{Z_i}\, Y_{n,0}^{(A_i - Z_i)}\, \frac{G_i(T)\, A_i^{3/2}}{2^{A_i}} \left(\frac{\rho}{m_b}\right)^{A_i - 1} \times \left(\frac{2\pi\hbar^2}{m_b k_{\rm B} T}\right)^{3(A_i-1)/2} e^{{\rm BE}_i/k_{\rm B}T}\,, \qquad (2)$$

with m_b and n_b baryon mass and number density, A_i and Z_i mass and atomic numbers of the i-th isotope

[2] We take the results of this simulation, where the BH collapse occurs around $t \simeq 10$ ms postmerger, as a representative history of disk ejecta. The general properties of disks and disk ejecta are found to be relatively stable against variations in the properties of the compact binary or numerical prescriptions (*e.g.* EoS, effective viscosity, neutrino treatment), as long as the BH collapse occurs in a timescale of $\mathcal{O}(10)$ ms (Fernández & Metzger 2013; Just et al. 2021, 2023; Camilletti et al. 2024).

and n_i and BE_i its number density and total binding energy. Here, $G_i(T)$ is the internal partition function of the nucleus i at temperature T. The two conditions $\sum_i A_i Y_i = 1$ and $\sum_i Z_i Y_i = Y_e$, with Y_e electron fraction, constrain the NSE composition, which thus depends on ρ, T and Y_e. See Lippuner & Roberts (2017) for details about `SkyNet`'s implementation of Eq. (2). The isotopic mass fractions can be calculated from the element abundances via $X_i = A_i Y_i$.

To calculate the specific energy deposition in Eq. (1), we independently thermalize the different contributions to $\dot{\epsilon}_{\rm nucl} = \dot{\epsilon}^{\gamma}_{\rm nucl} + \dot{\epsilon}^{\alpha}_{\rm nucl} + \dot{\epsilon}^{\beta}_{\rm nucl} + \dot{\epsilon}^{\rm oth}_{\rm nucl}$ coming from γ rays, α particles, electrons, and other nuclear reactions products. We compute the fraction of energy thermalized by the emission of γ-rays as

$$\dot{\epsilon}^{\gamma}_{\rm nucl}(t) = \sum_j f^{\gamma}_j(t) \frac{\langle E^{\gamma}_j \rangle Y_j(t)}{\tau_j \, m_p} \,, \tag{3}$$

with j isotope index and m_p proton mass. The average lifetimes τ_j and the mean energy $\langle E^{\gamma}_j \rangle$ released by each of these nuclei in γ-rays via a radioactive decay are taken from the ENDF/B-VIII.0 database[3] (Brown et al. 2018). The thermalization factor $f^{\gamma}_j(t)$ is calculated, as in Hotokezaka & Nakar (2019); Combi & Siegel (2023a), starting from the detailed composition of the ejecta and the same effective opacity tables from the NIST-XCOM catalogue[4] (Berger et al. 2010) used in Barnes et al. (2016). For the energy injected in electrons and α particles and their thermalization factors, we use the analytic expressions of Kasen & Barnes (2019). Neutrinos from β-decays do not deposit energy into the system, while fission fragments and daughter nuclei tend to thermalize very efficiently (Barnes et al. 2016). We approximate this behavior by assuming that half of the remaining (non-thermalized) heating rate from `SkyNet` is deposited into the ejecta.

2.4. *Jet Energy Deposition*

We consider a jet model following the "thermal bomb" prescription of Morozova et al. (2015). Essentially, an extra energy term is added to the RHS of Eq. (1) for the innermost shells of the ejecta during a chosen time interval. The thermal bomb parameters are fixed assuming that the released isotropic energy from the sGRB is proportional to the kinetic energy of the structured jet described by Ghirlanda et al. (2019), $E_{\rm iso}(\theta) = E_0/[1 + (\theta/\theta_j)^{5.5}]$, with θ_j jet's opening angle. The total energy E_j released by the jet is related to $E_{\rm iso}$ by $E_{\rm iso} = (4\pi/\Delta\Omega_j)E_j$, where $\Delta\Omega_j = 2\pi(1 - \cos\theta_j)$ is the solid angle covered by the jet. We fix $\theta_j = 15$ degrees, within the range also explored in Hamidani et al. (2020) for the sGRB associated with GW170817. We simulate a jet with the same duration as the observed sGRB from Abbott et al. (2017c), $\Delta t_j = 100$ ms. We launch the jet at $t = 200$ ms and fix the parameter $E_0 = 10^{51}$ erg, to be compatible with the isotropic luminosity range given by Hamidani et al. (2020). Their Figure 9 shows that, in the case of GRB 170817A, choosing the isotropic luminosity to be $L_{\rm iso} \sim 10^{52}$ erg/s constrains the jet to be launched no more than 300 ms after merger.

[3] https://www-nds.iaea.org/exfor/endf.htm

[4] https://www.nist.gov/pml/xcom-photon-cross-sections-database

3. RESULTS

3.1. *Fluid Elements Composition Evolution*

Our simulation allows to self-consistently monitor the nuclear composition of the matter during its expansion. Figure 1 shows the time evolution of the mass fraction of protons, neutrons, rare earths and r-process peak elements (panels (*a*-*c*) and (*h*-*l*)), of the parameter $h(t)$ (see below, panels (*d*) and (*m*)) and of the electron fraction (panels (*e*) and (*n*)), together with the initial thermodynamic conditions of the ejecta (panels (*f*,*g*) and (*o*,*p*)), as a function of the Lagrangian mass coordinate. The left and right panels refer to two different angular sections, $\theta = 12$, 90 degrees. Mass shells with, respectively, $m \lesssim 48.45 \times 10^{-6}$ $\mathrm{M}_\odot$ and $m \lesssim 1.5 \times 10^{-3}$ $\mathrm{M}_\odot$ correspond to the wind, while larger values to the dynamical ejecta. In the latter, the entropy slightly increases towards the outer shells, where a high entropy, low mass tail is observed at all angles. Material with low initial electron fractions, $Y_{e,0} < 0.22$, is found in the outer regions of the ejecta and, for $m \sim 2.5 \times 10^{-3}$ $\mathrm{M}_\odot$, around the equatorial plane. During the evolution, the electron fraction raises to $Y_e > 0.22$ for almost every mass shell at around $t \sim 1$ s due to the β-decays following the neutron captures and neutron freeze-out

The color maps in panels (*d*) and (*m*) of Fig. 1 show the evolution of the parameter

$$h(t) \equiv \log_{10}\left(\frac{\rho(t)}{\rho_{\texttt{SkyNet}}(t \,|\, \rho_0, \tau_0)}\right) . \tag{4}$$

The density evolution for the homologous expansion $\rho_{\texttt{SkyNet}}$ is parametrized by the initial density ρ_0 and expansion timescale τ_0 as defined in Eq. (1) of Lippuner & Roberts (2015). The same homologous expansion is used by Perego et al. (2022); Wu et al. (2022) for the time-domain fitting of the heating rates. Positive (negative) values of h indicate regions of the $t - M$ plane where the mass shells are characterized by higher (lower) densities than the one predicted by the simple homologous model. Shells where h is constant in time are

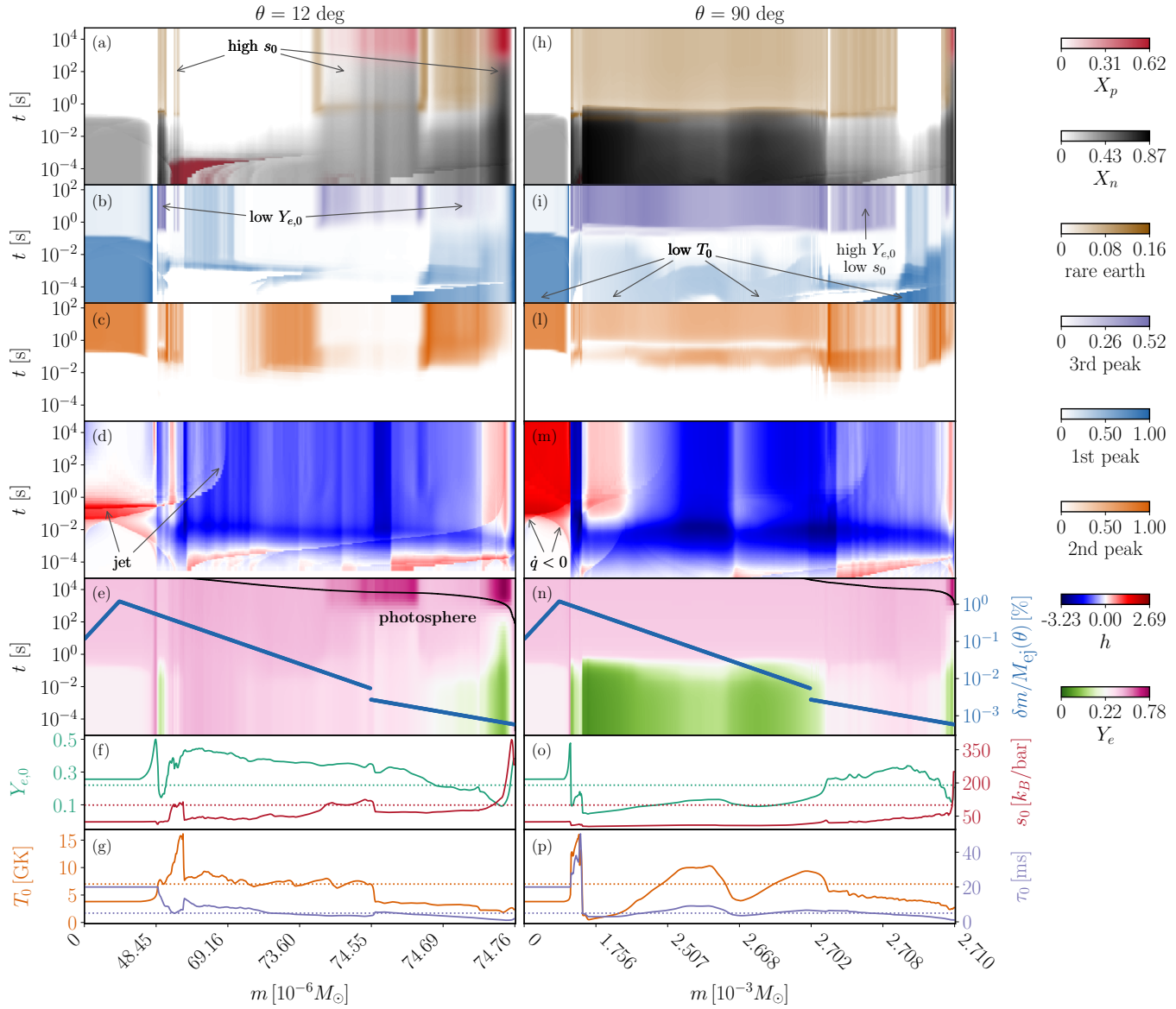

Figure 1. Evolution of the ejecta composition for every mass shell of the angular sections $\theta \simeq 12, 90$ degrees (first and second column respectively). The x-axis indicates the Lagrangian mass coordinate. The color maps in panels (*a*-*c*) and (*h*-*l*) represent the mass fractions of neutrons (in gray), protons (red), first (blue), second (orange), and third (purple) r-process peak elements, and rare earths (brown). Panels (*d*, *m*) and (*e*, *n*) show the evolution of the parameter $h(t)$ defined in (4) (blue to red) and of the electron fraction (green to pink), respectively. In (*e*) and (*n*) we also plot the fraction of the total mass ejected in the considered angular section included in each mass shell (in blue, since mass is not uniformly distributed within the shells) and the position of the photosphere (in black). Subplots (*f*-*g*) and (*o*-*p*) show the initial values of Y_e, s, T, τ as a function of the included mass. The horizontal dotted lines indicate the limit values of $Y_{e,0} = 0.22$, $s_0 = 100\,k_{\rm B}$/baryon, $T_0 = 7$ GK, and $\tau_0 = 5$ ms.

expanding homologously. If $h \neq 0$, the evolution happens on a curve $\rho_{\texttt{SkyNet}}(t\,|\,\rho_0', \tau_0')$ different from the one associated with the values of ρ_0, τ_0 of the considered mass shell. This happens for most of the shells in our simulation for $t \gtrsim 100$ s, in agreement with the results of Rosswog et al. (2014). We identify a deviation of approximately three orders of magnitude between our numerical solution and the specific homologous expansion $\rho_{\texttt{SkyNet}}(t\,|\,\rho_0, \tau_0)$. As commented below, such different homologous expansions can lead to inconsistent nucleosynthesis predictions. At $t \sim 100$ ms, a sudden increase of h is observed in the disk ejecta. It corresponds to the absorption of energy from the fluid to the NN ($\dot{\epsilon}_{\rm nucl} < 0$) that slows down the matter expansion. This effect is genuinely due to the coupling between the NN and hydrodynamics, and it cannot be reproduced by

offline analyses. In the polar regions, a further compression at $t \sim 200$ ms, followed by a more rapid expansion, is caused by the extra energy deposited by the jet.

Panels (*a-c*) and (*h-l*) of Fig. 1 show the evolution of the cumulative mass fractions of groups of selected isotopes. Consistently throughout the ejecta, shells with $Y_{e,0} \lesssim 0.22$ produce first peak elements (embedded in a see of free neutrons) within $t \lesssim 10^{-4}$ s. On a time scale of a second, these nuclei are converted to second and third peak elements and a small fraction of rare earths. At $T_0 \gtrsim 7$ GK, most of the ejecta is initially composed of free neutrons and protons (their ratio depending on the initial electron fraction) and light elements, which will act as seeds for r-process nucleosynthesis. In regions where $T_0 \lesssim 7$ GK, the initial temperature is low enough in certain mass shells (see the arrows in panel (i)) to make the binding energy term in Eq. (2) strongly affect the NSE composition. Hence, a significant fraction of first peak elements is already formed at $t = 0$ and can be directly used as r-process seeds. This can ease the heavy elements production and, in some cases, partially induce strong r-processes even for $Y_e \gtrsim 0.22$ (see for example the high $Y_{e,0}$, low s_0 third peak production in the $\theta = 90$ degrees case). However, first peak elements are not consistently produced by NSE at $T \lesssim 7$ GK. In some inner parts of the angular shell $\theta = 12$ degrees, close to the transition temperature, the density is already low enough to prevent these elements to appear at $t = 0$.

High enough values of the initial entropy ($s_0 \gtrsim 100\,k_{\rm B}$/baryon) can lead to the production of rare earths, lanthanides and actinides even for intermediate values of the initial electron fraction, $0.22 \lesssim Y_e \lesssim 0.35$. This outcome is compatible with an α-rich freeze-out, characterized by a large neutrons to seed ratio (Just et al. 2015; Cowan et al. 2021). However, not all shells with high initial entropy are sites of strong r-process nucleosynthesis. This is clearly shown, for example, by the $\theta = 12$ degree angular section in the region $74.55 \lesssim m/(10^{-6}\ {\rm M}_\odot) \lesssim 74.69$. There, while the initial T_0, s_0 and τ_0 profiles are almost constant, only the detailed evolution of the local thermo- and hydrodynamics conditions determine with accuracy the subsequent nucleosynthesis yields. When strong r-processes are activated, free neutrons are efficiently consumed, strongly reducing the final abundance of free protons (see panel (*a*)). Note that the decreasing of $Y_{e,0}$ in those mass shells cannot justify the differences in the final abundances: an analogous reduction of $Y_{e,0}$ in the lower mass shells at $m \lesssim 74.55 \times 10^{-6}$ M$_\odot$ has the opposite effect. Furthermore, the jumps in T_0, s_0 and τ_0 at around $m \simeq 74.55 \times 10^{-6}$ M$_\odot$ do not significantly affect the r-process nucleosynthesis.

For low entropies, $s_0 \lesssim 100\,k_{\rm B}$/baryon, and intermediate values of the initial electron fractions, $0.22 \lesssim Y_{e,0} \lesssim 0.35$, the fewer free neutrons are rapidly captured by seed nuclei, and only second peak elements are produced at the end of the nucleosynthesis. Note again the exception represented by the shells at around $m \simeq 2.708 \times 10^{-3}$ M$_\odot$ in the equatorial section. At the high $Y_{e,0} \gtrsim 0.35$ reached in the polar section, weak r-processes occur at low entropy and only first peak elements can be produced.

Extremely high values of the initial entropy, $s_0 \gtrsim 200\,k_{\rm B}$/baryon, can be reached in the outermost shells of the ejecta. Despite the large neutrons to seed ratio, neutron capture is not effective in the fast ejecta tail ($v \gtrsim 0.6$). Nucleosynthesis is therefore hindered. In this rarefied environment, most of the neutrons remain free after the r-process freeze-out and start β-decaying on a timescale of $t \sim 10$ minutes, while crossing the photosphere, which position is tracked in panels (*e*) and (*n*). This can power a UV/blue kilonova precursor on the hours timescales, as discussed below Fig. 4. After 10^4 s, no heavy element is produced, and free protons dominate the final matter composition. This is reflected in the high final electron fractions of these shells. If the strong rise in entropy is combined with an initial electron fraction $Y_{e,0} \gtrsim 0.35$, all neutrons are initially bound in stable first peak elements. In these outer regions, the composition remains essentially frozen. We can thus predict a negligible nuclear contribution to the kilonova light curves from these shells throughout the ejecta evolution, regardless of the photosphere position.

The qualitative changes in the nucleosynthesis patterns caused by the jet are negligible. The only quantitative effect observed on the mass fractions depicted in Fig. 1 is a very slight delay in the production of second r-process peak elements in the innermost shells of the polar sections. No significant effects arise in the regions near the equatorial plane, as the jet energy is negligible at low latitudes, and we do not account for the coupling between different angular sections.

In summary, our results indicate that it is not possible to predict the final nucleosynthesis yields based on the initial thermodynamic conditions of the ejecta solely.

3.2. *Global Nucleosynthesis Yields*

We calculate the global abundances $\langle Y_i \rangle$ as mass-weighted averages over all the mass shells of all the angular sections. In Fig. 2, we show the matter composition at $t \simeq 5 \times 10^4$ s. Except for small modifications due to long lived α-decaying isotopes, this is a good representation of the final r-process nucleosynthesis yields. All the r-process peaks and in part rare earths are pro-

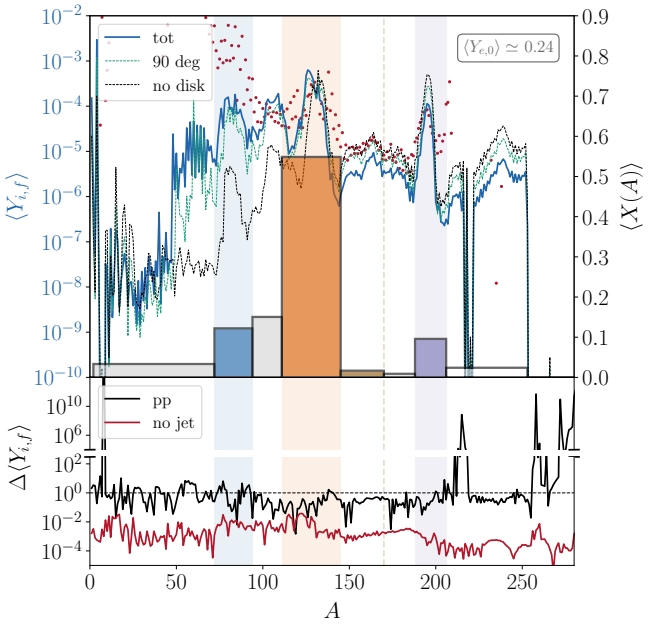

Figure 2. Global r-process nucleosynthesis yields at $t \simeq 5 \times 10^4$ s. Top panel: in blue, the final global abundances $\langle Y_{i,f} \rangle$. In green and black, the results obtained including only the matter emitted at $\theta = 90$ degrees and including or not the disk ejecta. Red dots represent the Solar system abundances (Lodders 2003) scaled to match the average value of the second peak. The histogram shows, for the complete simulation, the global cumulative mass fractions $\langle X(A) \rangle$ of selected groups of elements; in particular, first (blue), second (orange) and third (purple) r-process peaks and rare-earths (brown). We report the initial value of the average electron fraction of the ejecta in the top right corner of the plot. Bottom panel: in black, relative difference for the no-disk case between our results and the one obtained with the method described in Perego et al. (2022), see Eq. (5); in red, analogous comparison between the results of the complete simulation with and without the jet.

duced. This is expected, as matter is mostly ejected along the equatorial plane, where the neutron-rich dynamical ejecta keeps the global, initial average electron fraction at $\langle Y_{e,0} \rangle \simeq 0.24$. A detailed inspection of the angular profiles shows that the polar sections, characterized by an higher Y_e, do not significantly produce elements beyond the second peak. By comparing the results of our complete model with the ones obtained by excluding the late disk wind, we establish that most of the elements with $50 \lesssim A \lesssim 130$ (in particular first and second peaks and iron group isotopes) are produced by the disk wind. Heavy elements production is instead already saturated in the dynamical ejecta. These results are in agreement with Martin et al. (2015); Cowan et al. (2021); Curtis et al. (2023); Chiesa et al. (2024).

In the bottom panel of Fig. 2 we show the final value of the relative difference

$$\Delta \langle Y_i^{pp} \rangle = \frac{|\langle Y_i \rangle - \langle Y_i^{pp} \rangle|}{\min\left(\langle Y_i \rangle, \langle Y_i^{pp} \rangle\right)} \,. \tag{5}$$

between our results and the predictions $\langle Y_i^{pp} \rangle$ obtained with the method described in Perego et al. (2022). The latter work computes nucleosynthesis in post-processing using the same NN and homologously expanding ejecta profiles. Significative deviations between the two models are found for all values of A.

Figure 3 shows the evolution of the abundances for free protons and neutrons and a few selected isotopes. The r-process nucleosynthesis takes place between $t \sim 10^{-2}$ s and $t \sim 1$ s, when the first drop in $\langle Y_n \rangle$ occurs. The plateau at $Y_n \simeq 10^{-4}$ in the top panel indicates the presence of regions of the ejecta where the material undergoes incomplete neutron burning. The second drop in the abundance of neutrons at $t \sim 10$ minutes, connected with an increase in the proton fraction, is due to free neutrons β-decays. A closer look at the innermost shells reveals some oscillations on Y_n for $t \gtrsim 1$ s. We interpret these as the effects of the combination of neutron emissions and the often following β-decays. The analysis of some specific shells in single angular sections shows qualitative features similar to those discussed in Perego et al. (2022). However, a direct comparison between the two models shows discrepancies up to four orders of magnitude in the abundance evolution of several isotopes, see panel (d). This highlights the necessity of coupling the NN with the radiation-hydrodynamic evolution of the ejecta to get consistent predictions about the nucleosynthesis process.

The initial global abundance of ^{4}He is of the order of 10^{-2} because of shells undergoing α-rich freeze out. This isotope is partially consumed at early times to construct heavier elements, *e.g.* ^{88}Sr. In the innermost shell, it is produced again during the r-process nucleosynthesis by α-decays of the freshly produced heavy, neutron-rich elements, see panel (b). These regions are crossed by the jet, which produces a rapid increase in the abundances of protons and deuterium at $t \simeq 200$ ms. ^{88}Sr is initially strongly suppressed, but it rises enough at early times to effectively act as a seed for r-process nucleosynthesis. At late times this element is produced again as part of the first peak by β-decaying neutron-rich isotopes. This is particularly evident in panel (b) of Fig. 3. We also show the abundance of ^{56}Fe as representative of the most bounded nuclei around the iron peak. Its initial formation is favored by its high binding energy. Like strontium, ^{56}Fe acts as a seed nucleus, but it is only partially produced again by later nuclear reactions.

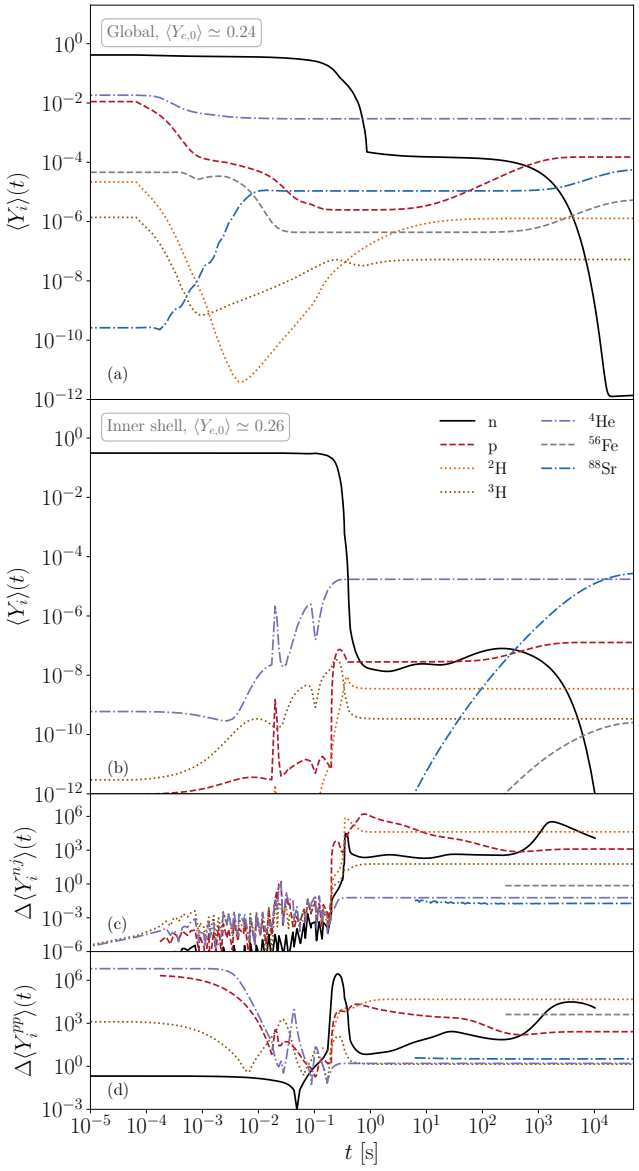

Figure 3. Evolution of a few selected abundances. Panels (a) and (b): global results and innermost shell; at the top left corner, we report the initial values of the electron fraction. Panel (c): comparison between the results obtained with the complete simulation and without the jet using an expression analogous to Eq. (5). Panel (d): comparison between our results for the innermost shells and the prediction obtained from the procedure outlined in Perego et al. (2022), see Eq. (5). In panels (c, d), the results are only shown for times $\hat{t}$ such that $\langle Y_i\rangle(\hat{t}) > 10^{-12}$.

The additional energy released by the jet significantly affects only a fraction of the inner shells at the highest latitudes. The mass involved is a too small fraction of the ejecta to yield visible effects on the global results presented in Fig. 2 and 3. In particular, the final

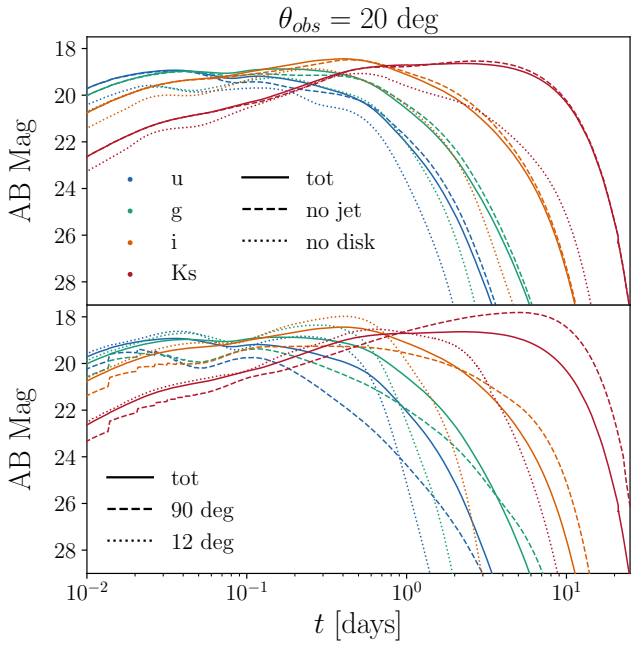

Figure 4. AB apparent magnitudes predicted by our simulation for the Gemini bands u, g, i and K_s for an observation angle of $\theta = 20$ degrees. Top panel: results from the complete simulation (solid line) and by excluding the jet (dashed lines) or the disk component (dotted lines). Bottom panel: results from the complete simulation (solid line) and the isotropized $\theta = 12, 90$ degrees angular sections (dotted and dashed lines respectively).

nuclear yields are compatible to few percents between the complete simulations with and without the jet (see the bottom panel of Fig. 2). Nevertheless, the examination of the nucleosynthesis within the inner shells of the polar sections reveals some modifications of the final abundances for the selected elements of Fig. 3, see panel (c). The sudden acceleration induced by the jet slows neutron captures down, therefore leaving, at the end of the nucleosynthesis, more free β-decaying neutrons and, consequently, free protons. The faster dynamics also inhibits the burning of light elements, leading to an increase in the abundance of hydrogen isotopes at the end of the simulation.

3.3. *Light curves*

In Fig. 4 we show the kilonova light curves predicted by our model for an observation angle of $\theta = 20$ degrees and for a few selected UV/visible/IR bands. At $t \sim 3 \times 10^{-2}$ days, all the simulations show a bump in the blue light curves, compatible with the UV precursor predicted in Combi & Siegel (2023a) to be powered by β-decaying free neutrons.

The disk is predicted to contribute to the blue component of the kilonova due to its lower opacity, see

e.g. (Metzger & Fernández 2014; Siegel 2019; Curtis et al. 2024). However, at all angles, the photosphere enters the disk region only at late times ($t \sim 10$ days), when the temperature drop has already made the disk spectra red. Essentially, the dynamical ejecta acts as a curtain, preventing the disk to significantly boost the blue part of the kilonova. Correspondingly, in the top panel of Fig. 4, all the curves show an analogous decrease in their luminosity, when the disk is excluded, only due to the removal of part of the ejected mass. The bottom panel of Fig. 4 shows that, around the equator, the opaque lanthanide curtain associated with the dynamical ejecta produces a red kilonova. The blue components of the spectra become dominant at higher latitudes, suggesting a main contribution to the blue kilonova from the angular sections around the disk edge, where a still significative mass of relatively neutron-poor material is ejected.

The jet slightly increases the early ($t \sim 0.1 - 1$ days) light curves in all bands. The effect is stronger and can be seen earlier for higher frequencies. This is due to the extra energy input increasing the temperature and thus leading to a bluer and brighter emission. The consequently more efficient matter cooling causes the temperature to decrease faster, thus reducing the magnitudes at later times with respect to the jet-free case. A similar effect is discussed in Nativi et al. (2020), where the jet is found to clear a significant fraction of the lanthanide curtain.

4. CONCLUSIONS

In this work we investigated the nucleosynthesis process in a BNSM ejecta by means of a 2-dimensional (ray-by-ray) radiation-hydrodynamics simulation incorporating an online NN.

Our results challenge the widely used approach of predicting r-process nucleosynthesis from isolated fluid elements. Figure 1 illustrates that it is not possible to fully predict the detailed distribution of the (final) nucleosynthesis yields solely from the initial thermodynamic conditions of a set of fluid elements. Moreover, the most commonly employed approximations for homologous expansions fail to capture the asymptotic hydrodynamic evolution of the unbound material. Therefore, even estimates for the nuclear heating rate obtained by post-processing isolated fluid elements, see *e.g.* (Rosswog et al. 2014; Wanajo 2018; Wu et al. 2022; Rosswog & Korobkin 2022; Collins et al. 2023; Shingles et al. 2023; Ricigliano et al. 2023), may lead to inconsistent results. To get a consistent picture of the ongoing nuclear processes, the effects related to radiation transfer and ejecta self-interaction must be taken into account. Furthermore, nuclear reactions play a preponderant role in supplying or removing energy to the expanding material. Providing a radiation-hydrodynamic simulation of the ejecta from compact binary mergers with an online NN thus appears crucial also for improving the realism of the hydrodynamic evolution itself.

Some of the outer layers of the ejecta primarily consist of β-decaying free neutrons, see in Fig. 1; this confirms the findings of de Jesús Mendoza-Temis et al. (2015); Radice et al. (2018a). As suggested by Metzger et al. (2015); Fernández et al. (2019); Combi & Siegel (2023a), such a high-velocity ($\tau \lesssim 5$ ms), neutron-rich envelope can power a bright UV/blue kilonova precursor over timescales of hours. In our simulations, having a very rapidly expanding ejecta is not sufficient to prevent the production of third-peak elements and to light the kilonova precursor. Very high entropies, $s \gtrsim 100\, k_{\rm B}$/baryon, are also required to leave a strong abundance of free neutrons after the r-process freeze-out. However, once these conditions are met, the decays of free neutrons outside of the photosphere allow for a visible EM signature on the kilonova light curves.

From a qualitative point of view, our averaged results for nucleosynthesis yields in Fig. 2 align with other predictions in the literature, *e.g.* (Cowan et al. 2021; Perego et al. 2021). Our analysis reveals a connection between the production of light (first peak and below) and third-peak elements with late disk and dynamical ejecta respectively, in agreement with Martin et al. (2015); Cowan et al. (2021). Figure 4 shows that the outer lanthanides curtain shields the radiation produced by the inner disk ejecta, thus preventing them to give the significant contribution to the blue component of the kilonova predicted by Metzger & Fernández (2014); Siegel (2019); Curtis et al. (2024). The polar part of our ejecta evolves from higher Y_e and produces very few heavy r-process elements; this is consistent with the link discussed in Kasen et al. (2017); Tanaka et al. (2017); Nicholl et al. (2017); Perego et al. (2017) between the blue kilonova component and these sections of the unbound material.

We compared the time evolution of the nuclear abundances from previous work that utilized the same NN but in post-processing (Perego et al. 2022). We find significant quantitative differences for some of the analyzed elements (a qualitative agreement is found only for some specific shells in our simulation). In particular, in the innermost part of the ejecta, we find discrepancies of up to four orders of magnitudes in the final abundances of all the elements represented in Fig. 3, except for ^{3}H, ^{4}He and ^{88}Sr. The differences are due to the coupling of the NN with the radiation-hydrodynamic evolution. This

also affects the predictions for the global nucleosynthesis yields. We find a deviation of a factor $\gtrsim 10\%$ consistently for all r-process peaks (see the bottom panel of Fig. 2).

The inclusion of an extra energy term mimicking a jet only affects the dynamic evolution of the polar regions of the ejecta, without altering the global, qualitative predictions of the r-process nucleosynthesis.

Our work will be extended and improved in several directions. We aim at implementing an improved thermalization of charged particles and a more realistic opacity treatment based on the complete, tracked information about matter composition. A following paper will report a systematic investigation of kilonova light curves using hundreds-of-milliseconds long numerical-relativity profiles and those improved thermalization and opacity models. Finally, the methods developed here will be ported to 3-dimensional simulations.

FM acknowledges support from the Deutsche Forschungsgemeinschaft (DFG) under Grant No. 406116891 within the Research Training Group RTG 2522/1. FM also acknowledges ECT* for organizing the MICRA2023 workshop and TIFPA for their invitation to Trento in December 2023. Both occasions were sites of useful discussions. SB knowledges funding from the EU Horizon under ERC Consolidator Grant, no. InspiReM-101043372 and from the Deutsche Forschungsgemeinschaft, DFG, project MEMI number BE 6301/2-1. The work of AP is partially funded by the European Union under NextGenerationEU, PRIN 2022 Prot. n. 2022KX2Z3B. DR acknowledges funding from the U.S. Department of Energy, Office of Science, Division of Nuclear Physics under Award Number(s) DE-SC0021177 and DE-SC0024388, and from the National Science Foundation under Grants No. PHY-2011725, PHY-2020275, PHY-2116686, and AST-2108467.

Simulations were performed on the ARA and DRACO clusters at Friedrich Schiller University Jena, on the supercomputer SuperMUC-NG at the Leibniz- Rechenzentrum (LRZ, www.lrz.de) Munich, and on the national HPE Apollo Hawk at the High Performance Computing Center Stuttgart (HLRS). The ARA cluster is funded in part by DFG grants INST 275/334-1 FUGG and INST 275/363-1 FUGG, and ERC Starting Grant, grant agreement no. BinGraSp-714626. The authors acknowledge the Gauss Centre for Supercomputing e.V. (www.gauss-centre.eu) for funding this project by providing computing time on the GCS Supercomputer SuperMUC-NG at LRZ (allocations `pn36ge` and `pn36jo`). The authors acknowledge HLRS for funding this project by pro- viding access to the supercomputer HPE Apollo Hawk under the grant number INTRHYGUE/44215.

REFERENCES

Abbott, B. P., et al. 2017a, Phys. Rev. Lett., 119, 161101, doi: 10.1103/PhysRevLett.119.161101

—. 2017b, Astrophys. J., 848, L12, doi: 10.3847/2041-8213/aa91c9

—. 2017c, Astrophys. J. Lett., 848, L13, doi: 10.3847/2041-8213/aa920c

Arcones, A., & Thielemann, F.-K. 2023, Astron. Astrophys. Rev., 31, 1, doi: 10.1007/s00159-022-00146-x

Barnes, J., Kasen, D., Wu, M.-R., & Martinez-Pinedo, G. 2016, Astrophys. J., 829, 110, doi: 10.3847/0004-637X/829/2/110

Bauswein, A., Goriely, S., & Janka, H.-T. 2013, Astrophys.J., 773, 78, doi: 10.1088/0004-637X/773/1/78

Beloborodov, A. M. 2003, Astrophys. J., 588, 931, doi: 10.1086/374217

Berger, M., et al. 2010. http://physics.nist.gov/xcom

Bernuzzi, S. 2020, Gen. Rel. Grav., 52, 108, doi: 10.1007/s10714-020-02752-5

Brown, D. A., et al. 2018, Nucl. Data Sheets, 148, 1, doi: 10.1016/j.nds.2018.02.001

Camilletti, A., Perego, A., Guercilena, F. M., Bernuzzi, S., & Radice, D. 2024, Phys. Rev. D, 109, 063023, doi: 10.1103/PhysRevD.109.063023

Chiesa, L., Perego, A., & Guercilena, F. M. 2024, Astrophys. J. Lett., 962, L24, doi: 10.3847/2041-8213/ad236e

Collins, C. E., Bauswein, A., Sim, S. A., et al. 2023, Mon. Not. Roy. Astron. Soc., 521, 1858, doi: 10.1093/mnras/stad606

Combi, L., & Siegel, D. M. 2023a, Astrophys. J., 944, 28, doi: 10.3847/1538-4357/acac29

—. 2023b, Phys. Rev. Lett., 131, 231402, doi: 10.1103/PhysRevLett.131.231402

Coulter, D. A., et al. 2017, Science, doi: 10.1126/science.aap9811

Cowan, J. J., Sneden, C., Lawler, J. E., et al. 2021, Rev. Mod. Phys., 93, 15002, doi: 10.1103/RevModPhys.93.015002

Curtis, S., Bosch, P., Mösta, P., et al. 2024, Astrophys. J. Lett., 961, L26, doi: 10.3847/2041-8213/ad0fe1

Curtis, S., Miller, J. M., Frohlich, C., et al. 2023, Astrophys. J. Lett., 945, L13, doi: 10.3847/2041-8213/acba16

Cyburt, R. H., Amthor, A. M., Ferguson, R., et al. 2010, Astrophys. J. Suppl., 189, 240, doi: 10.1088/0067-0049/189/1/240

de Jesús Mendoza-Temis, J., Wu, M.-R., Martinez-Pinedo, G., et al. 2015, Phys. Rev., C92, 055805, doi: 10.1103/PhysRevC.92.055805

Eichler, D., Livio, M., Piran, T., & Schramm, D. N. 1989, Nature, 340, 126, doi: 10.1038/340126a0

Fernández, R., & Metzger, B. D. 2013, Mon. Not. Roy. Astron. Soc., 435, 502, doi: 10.1093/mnras/stt1312

Fernández, R., Tchekhovskoy, A., Quataert, E., Foucart, F., & Kasen, D. 2019, Mon. Not. Roy. Astron. Soc., 482, 3373, doi: 10.1093/mnras/sty2932

Ghirlanda, G., et al. 2019, Science, 363, 968, doi: 10.1126/science.aau8815

Goriely, S. 2015, Eur. Phys. J. A, 51, 22, doi: 10.1140/epja/i2015-15022-3

Goriely, S., Bauswein, A., & Janka, H.-T. 2011, Astrophys. J. Lett., 738, L32, doi: 10.1088/2041-8205/738/2/L32

Hamidani, H., Kiuchi, K., & Ioka, K. 2020, Mon. Not. Roy. Astron. Soc., 491, 3192, doi: 10.1093/mnras/stz3231

Hotokezaka, K., & Nakar, E. 2019, doi: 10.3847/1538-4357/ab6a98

Janiuk, A. 2014, Astron. Astrophys., 568, A105, doi: 10.1051/0004-6361/201423822

Just, O., Bauswein, A., Pulpillo, R. A., Goriely, S., & Janka, H. T. 2015, Mon. Not. Roy. Astron. Soc., 448, 541, doi: 10.1093/mnras/stv009

Just, O., Goriely, S., Janka, H.-T., Nagataki, S., & Bauswein, A. 2021, Mon. Not. Roy. Astron. Soc., 509, 1377, doi: 10.1093/mnras/stab2861

Just, O., Vijayan, V., Xiong, Z., et al. 2023, Astrophys. J. Lett., 951, L12, doi: 10.3847/2041-8213/acdad2

Kasen, D., & Barnes, J. 2019, Astrophys. J., 876, 128, doi: 10.3847/1538-4357/ab06c2

Kasen, D., Metzger, B., Barnes, J., Quataert, E., & Ramirez-Ruiz, E. 2017, Nature, doi: 10.1038/nature24453

Korobkin, O., Rosswog, S., Arcones, A., & Winteler, C. 2012, Mon. Not. Roy. Astron. Soc., 426, 1940, doi: 10.1111/j.1365-2966.2012.21859.x

Lippuner, J., & Roberts, L. F. 2015, Astrophys. J., 815, 82, doi: 10.1088/0004-637X/815/2/82

—. 2017, Astrophys. J. Suppl., 233, 18, doi: 10.3847/1538-4365/aa94cb

Lodders, K. 2003, Astrophys. J., 591, 1220, doi: 10.1086/375492

Martin, D., Perego, A., Arcones, A., et al. 2015, Astrophys. J., 813, 2, doi: 10.1088/0004-637X/813/1/2

Metzger, B. D., Bauswein, A., Goriely, S., & Kasen, D. 2015, Mon. Not. Roy. Astron. Soc., 446, 1115, doi: 10.1093/mnras/stu2225

Metzger, B. D., & Fernández, R. 2014, Mon.Not.Roy.Astron.Soc., 441, 3444, doi: 10.1093/mnras/stu802

Morozova, V., Piro, A. L., Renzo, M., et al. 2015, Astrophys. J., 814, 63, doi: 10.1088/0004-637X/814/1/63

Musolino, C., Duqué, R., & Rezzolla, L. 2024. https://arxiv.org/abs/2402.11009

Nativi, L., Bulla, M., Rosswog, S., et al. 2020, Mon. Not. Roy. Astron. Soc., 500, 1772, doi: 10.1093/mnras/staa3337

Nedora, V., Bernuzzi, S., Radice, D., et al. 2021, Astrophys. J., 906, 98, doi: 10.3847/1538-4357/abc9be

Nicholl, M., et al. 2017, Astrophys. J., 848, L18, doi: 10.3847/2041-8213/aa9029

Paczynski, B. 1986, Astrophys. J., 308, L43

Perego, A., Bernuzzi, S., & Radice, D. 2019, Eur. Phys. J., A55, 124, doi: 10.1140/epja/i2019-12810-7

Perego, A., Radice, D., & Bernuzzi, S. 2017, Astrophys. J., 850, L37, doi: 10.3847/2041-8213/aa9ab9

Perego, A., Thielemann, F. K., & Cescutti, G. 2021, in Handbook of Gravitational Wave Astronomy, 1, doi: 10.1007/978-981-15-4702-7_13-1

Perego, A., et al. 2022, Astrophys. J., 925, 22, doi: 10.3847/1538-4357/ac3751

Radice, D., & Bernuzzi, S. 2023a, Astrophys. J., 959, 46, doi: 10.3847/1538-4357/ad0235

Radice, D., & Bernuzzi, S. 2023b, in 15th International Conference on Numerical Modeling of Space Plasma Flows. https://arxiv.org/abs/2310.09934

Radice, D., Bernuzzi, S., Perego, A., & Haas, R. 2022, Mon. Not. Roy. Astron. Soc., 512, 1499, doi: 10.1093/mnras/stac589

Radice, D., Galeazzi, F., Lippuner, J., et al. 2016, Mon. Not. Roy. Astron. Soc., 460, 3255, doi: 10.1093/mnras/stw1227

Radice, D., Perego, A., Hotokezaka, K., et al. 2018a, Astrophys. J. Lett., 869, L35, doi: 10.3847/2041-8213/aaf053

—. 2018b, Astrophys. J., 869, 130, doi: 10.3847/1538-4357/aaf054

Ricigliano, G., Perego, A., Borhanian, S., et al. 2023. https://arxiv.org/abs/2311.15709

Roberts, L. F., Lippuner, J., Duez, M. D., et al. 2017, Mon. Not. Roy. Astron. Soc., 464, 3907, doi: 10.1093/mnras/stw2622

Rosswog, S., Feindt, U., Korobkin, O., et al. 2017, Class. Quant. Grav., 34, 104001, doi: 10.1088/1361-6382/aa68a9

Rosswog, S., & Korobkin, O. 2022. https://arxiv.org/abs/2208.14026

Rosswog, S., Korobkin, O., Arcones, A., Thielemann, F. K., & Piran, T. 2014, Mon. Not. Roy. Astron. Soc., 439, 744, doi: 10.1093/mnras/stt2502

Savchenko, V., et al. 2017, Astrophys. J., 848, L15, doi: 10.3847/2041-8213/aa8f94

Schianchi, F., Gieg, H., Nedora, V., et al. 2023. https://arxiv.org/abs/2307.04572

Sekiguchi, Y., Kiuchi, K., Kyutoku, K., Shibata, M., & Taniguchi, K. 2016, Phys. Rev., D93, 124046, doi: 10.1103/PhysRevD.93.124046

Shibata, M., Fujibayashi, S., Hotokezaka, K., et al. 2017, Phys. Rev., D96, 123012, doi: 10.1103/PhysRevD.96.123012

Shingles, L. J., Collins, C. E., Vijayan, V., et al. 2023, Astrophys. J. Lett., 954, L41, doi: 10.3847/2041-8213/acf29a

Siegel, D. M. 2019, Eur. Phys. J. A, 55, 203, doi: 10.1140/epja/i2019-12888-9

Siegel, D. M., & Metzger, B. D. 2017, Phys. Rev. Lett., 119, 231102, doi: 10.1103/PhysRevLett.119.231102

Sprouse, T. M., Lund, K. A., Miller, J. M., McLaughlin, G. C., & Mumpower, M. R. 2023. https://arxiv.org/abs/2309.07966

Tanaka, M., et al. 2017, Publ. Astron. Soc. Jap., doi: 10.1093/pasj/psx121

Tanvir, N. R., et al. 2017, Astrophys. J., 848, L27, doi: 10.3847/2041-8213/aa90b6

Timmes, F. X., & Swesty, F. D. 2000, Astrophys. J. Suppl., 126, 501, doi: 10.1086/313304

Von Neumann, J., & Richtmyer, R. D. 1950, Journal of Applied Physics, 21, 232, doi: 10.1063/1.1699639

Wanajo, S. 2018, Astrophys. J., 868, 65, doi: 10.3847/1538-4357/aae0f2

Wanajo, S., Sekiguchi, Y., Nishimura, N., et al. 2014, Astrophys. J., 789, L39, doi: 10.1088/2041-8205/789/2/L39

Wu, Z., Ricigliano, G., Kashyap, R., Perego, A., & Radice, D. 2022, Mon. Not. Roy. Astron. Soc., 512, 328, doi: 10.1093/mnras/stac399

Zappa, F., Bernuzzi, S., Radice, D., & Perego, A. 2023, Mon. Not. Roy. Astron. Soc., 520, 1481, doi: 10.1093/mnras/stad107